J. Fluid Mech. (2010), *vol.* 660, *pp.* 87–113.
doi:10.1017/S0022112010002570

Experimental study of a tip leakage flow: wavelet analysis of pressure fluctuations

R. CAMUSSI[1]†, J. GRILLIAT[1], G. CAPUTI-GENNARO[1] AND M. C. JACOB[2]

[1]Department of Mechanical and Industrial Engineering, University of Roma Tre, Via della Vasca Navale 79, Rome, I-00146, Italy

[2]Centre Acoustique – LMFA UMR CNRS 5509, Ecole Centrale de Lyon, 36 Avenue Guy de Collongues, Lyon, F-69134 Ecully CEDEX, France

(Received 14 May 2009; revised 28 April 2010; accepted 29 April 2010; first published online 5 August 2010)

A wavelet-based conditional analysis of unsteady flow and sound signals highlights the role of intermittent perturbations both in the sound generation and the unsteady field of an aerofoil tip leakage flow experiment. It is shown how the most probable flow perturbations generated at the pressure side tip edge are convected through the gap and swept downstream along the suction side past the trailing edge tip corner, where they radiate sound. The nascent sound sources are identified and localized in the clearance between 40 % and 60 % of the chord. It is also found that the time dependence of the averaged intermittent structures scales with the inverse of the square root of the mean velocity and a physical interpretation based on a simple potential vortex model is proposed. The data are retrieved from an experiment that has been carried out at low Mach number ($Ma < 0.3$) in an anechoic test facility. A single motionless instrumented NACA 5510 aerofoil was mounted into the potential core of an open rectangular jet between two plates with an adjustable clearance. The tip leakage flow was ensured by the 5 % camber and a 15° angle of attack. A large database obtained by a variety of measurement techniques is thus available for the present analysis. More specifically, the conditional approach is applied to joint far field, wall pressure and particle image velocimetry (PIV) measurements. The wall pressure probes are located along the suction side tip edge and on the tip inside the gap, whereas the PIV plane is parallel to the mid-gap plane. Additional joint wall pressure and single hot-wire anemometry (HWA) measurements are also analysed with a hot-wire probe located near the trailing edge tip corner. The conditional averaging is triggered by high-energy wavelet events selected in a reference signal by setting a threshold to the so-called local intermittency measure.

Key words: aeroacoustics, separated flows, turbulent boundary layers

1. Introduction

Owing to recent progress in turbomachinery noise reduction technologies, fan noise has become one of the major noise sources for subsonic aircraft engines (Envia 2001). The contribution of broadband fan noise to the overall noise level is certain, especially during the landing phase where it accounts for as much as 50 %. Among other

† Email address for correspondence: camussi@uniroma3.it

broadband noise sources, rotor self-noise is composed of two major components: the noise generated when the blade boundary-layer disturbances interact with the trailing edge and the noise generated by the tip leakage flow interacting with the geometrical singularities of the blade tip (see e.g. Groeneweg *et al.* 1991; Rozenberg *et al.* 2007). Even though the physics of noise production at the trailing edge are nowadays quite well understood (see among others Amiet 1976; Howe 1978; Goldstein 1979; Casper & Farassat 2004; Roger & Moreau 2005; Moreau & Roger 2009), the tip leakage area is a region where broadband noise sources are suspected but remain difficult to identify and quantify.

From the aerodynamic viewpoint, the tip clearance flow field is an extremely complex three-dimensional unsteady viscous flow phenomenon. It has been found (see e.g. Bindon 1989; Storer & Cumpsty 1991) that a high-speed jet-like flow through the gap arises from the relative motion of the blade tip and the end wall and from the pressure difference across the blade tip. This flow, shed to the adjacent blade passage, eventually rolls up, forming a vortex-like structure that convects downstream (see also Vavra 1960). The resulting unsteady tip leakage vortex is a dominant feature of the flow field near the rotor blade tip region.

Tip leakage flows and their unsteady characteristics have been carefully studied in the past 50 years as they are known to reduce the aerodynamic efficiency, generate vibrations and even lead to structural damage in turbomachines. To acquire a better understanding of the tip leakage vortex physics, many aerodynamic studies have successfully revealed the principles of its formation and flow structure.

Among these studies, a series of experiments conducted on tip clearance flows in a compressor cascade by Muthanna & Devenport (2004), Wang & Devenport (2004), Wenger *et al.* (2004), Tang (2004) and Intratep (2006) appears to be of particular interest for the results discussed in this article, since they document the influence of various parameters onto the tip flow structure. Nevertheless, few efforts have concentrated on the problem related to the associated broadband noise-generation mechanisms.

Until recent years, tip clearance noise was not very well documented in the literature and besides the work of Dunne & Howe (1997), modelling efforts remained quite sparse for this difficult problem. There have been some studies about the magnitude of tip clearance noise in rotating rigs (Fukano & Takamatsu 1986; Fukano & Jang 2004) and some even tackled the problem of tip flow control (Neise 1976; Kameier & Neise 1997*a*, *b*; Khourrami & Choudari 2001; Corsini *et al.* 2005) including experimental and numerical investigations of instability mechanisms (März, Hah & Neise 2002). A careful study of Ganz *et al.* (1998) provides indications that the rotor blade tip interaction with the inlet boundary-layer turbulence is a significant source of noise and is strongly affected by the rotor tip clearance. However, their study also illustrated that it is quite difficult to separate the various phenomena occurring in the blade tip region in a representative fan rig: wall boundary-layer interaction with the blade tip, tip clearance flow, rotor tip wake/stator interactions. Because of the extremely complicated nature of these mechanisms, understanding of their interaction in the tip leakage flow and their contribution to the external noise level remains a challenging task.

Experimental investigations conducted by Ma (2003) on a linear cascade configuration show that, although large periodic fluctuations occur in the tip leakage flow downstream of the cascade, larger aperiodic components contain most of the turbulent energy. In his dissertation Ma (2003) used two-point correlation measurements and a linear stochastic estimation method to educe the structure of this aperiodic part: the velocity field associated with single point aperiodic velocity

fluctuations was found to consist of organized large-scale coherent structures. The presence of such coherent structures makes the estimated instantaneous velocity field significantly different from the phase-averaged periodic flow. The intermittent fluctuations are so intense in the tip leakage vortex region that the phase-averaged flow features are completely submerged by the aperiodic component. Microphone measurements also show that pressure mean square fluctuations downstream of the cascade are consistent with the velocity fluctuations, but the effectiveness of the identified coherent structures as acoustic sources was not investigated.

As mentioned above, in many attempts to address the question of tip clearance noise, difficulties arise from the fact that it could not clearly be distinguished among other noise sources in a representative fan rig. Tip clearance noise is indeed generated by various flow phenomena: one of the sources lies in the interaction between the blade and perturbations generated by the tip clearance flow in the vicinity of the blade. Although no experimental evidence for it was found in the literature, another possible source that is related to the former is likely to appear when the blade tip wake interacts with downstream located stator vane, just in the same manner as the whole rotor blade wake does.

For sufficiently large tip casing gaps, rotating instabilities appear in front of the rotor blades: Kameier & Neise (1997*a*, *b*) have shown that these instabilities play an important role in the blade tip noise generation by modifying the whole flow in the tip region. Although being more representative of realistic flow conditions, an experiment featuring all the aforementioned sources, allows neither proper investigation of the role of each contributor nor development of suitable models for each mechanism. To overcome these limitations, Grilliat *et al.* (2007) designed an experiment on a simplified configuration, which provided the data for the present study. This experiment was intentionally designed to focus on one of these mechanisms, the generation of self-noise by the tip leakage flow. A single NACA 5510 aerofoil is installed within an anechoic wind tunnel and, unlike some of the aforementioned cascade experiments, no relative motion between the aerofoil and the tip-facing wall is achieved since the aerofoil is mounted between two non-moving horizontal plates. A significant gap flow is obtained by selecting a cambered thick aerofoil that could be highly loaded. In this simple configuration, the side flow remains free, which allows us to carry out far-field measurements outside the flow in the medium at rest. As a result, differences can be expected when comparing the flow physics in the experiment to those of a real fan. In particular, as far as the noise generated by the tip leakage flow is concerned, it can be argued that in the absence of relative motion, the tip leakage perturbations are expected to remain closer to the blade and thus to generate more noise. Conversely, it can also be argued that the absence of neighbouring blades allows the tip leakage perturbations to be washed further away from the blade they originate from. As a result, it is unclear how the tip clearance flow of the single non-moving blade compares to that of a fan, but the conversion of aerodynamic perturbation into sound is likely to be qualitatively the same. Moreover, from an aeroacoustic viewpoint, this choice comes down to studying the resulting flow perturbations in the vicinity of the tip trailing-edge corner. Such a configuration is already very complex regarding the state of the art of aeroacoustic modelling activities. Most existing models are indeed two-dimensional: models based on Amiets approach are two-dimensional or quasi-two-dimensional (one dimension being large with respect to the other), whereas vortex models such as those developed by Dunne & Howe (1997) or Guo (1999) are two-dimensional in their essence.

Furthermore, the loss of realism is compensated by the possibility of obtaining a free far field in medium at rest, which is an important asset for broadband noise measurements. For all these reasons the present experimental study can be considered as relevant for the study of tip clearance self-noise. Finally, it is worth mentioning that this simplified configuration can be considered as generic for other applications, such as low-speed automotive fans, flap edges and slat/fuselage junctions on aerofoils or even in marine applications.

This work is devoted to the analysis of velocity and pressure data delivered in the Grilliat *et al.* (2007) experiment. The basic question, which represents the main motivation of this work, is whether a correlation exists between the dynamics of the unsteady intermittent structures forming in the tip leakage flow and both wall pressure fluctuations and acoustic emission. To this aim, a wavelet-based conditional technique has been developed and applied to the experimental data. Indeed, owing to the intrinsic intermittent nature of the phenomena under investigation, the wavelet transform appeared to be an optimal tool for its characterization. Details of the technique are given in the next section, where the so-called auto- and cross-conditioning procedures are described. A description of the experimental apparatus as well as of the measurement techniques is given in § 3. The main results pertaining to the aerodynamic and acoustic characterization of the tip leakage flow are discussed in § 4, while conclusions and final remarks are given in § 5.

2. Wavelet analysis and conditional statistics

During the last decades, wavelet analysis has been extensively used to treat random data obtained from both numerical simulations and experimental investigations of turbulent flows. In many of those applications, the use of wavelet transform was motivated by the need of separating intermittent events from the apparently nearly Gaussian turbulent background. Comprehensive reviews about the wavelet theory and its applications in turbulence can be found in many reference papers or books (see e.g. Mallat 1989; Meneveau 1991; Farge 1992).

The post-processing method adopted therein follows the procedure originally introduced by Camussi & Guj (1997), and successively applied to several turbulent flows as a tool for the identification of coherent structures (see e.g. Camussi & Guj 1999; Guj & Camussi 1999; Guj *et al.* 2003; Camussi & Di Felice 2006). In the present context, the procedure is applied to extract from wall and far-field pressure signals the most energetic non-periodic contributions localized in time and space and to detect the fluid dynamic structures responsible for such strong pressure fluctuations. The choice of the wavelet technique is motivated by the fact that the wavelet decomposition, unlike the Fourier transform, allows us to represent a generic signal simultaneously in terms of a translation time (t) and a resolution time scale (r), whose inverse is representative of the inverse of the frequency (f). This representation is accomplished by projecting the acquired signal over a basis of compact support functions obtained by dilations and translations of a so-called mother wavelet $\Psi(t)$ localized both in the time domain and in the transformed space. The mother wavelet can be considered as a bandpass filter of central frequency F_c, this parameter being actually a ratio between the width of the wavelet envelope and the pseudo-period of its oscillation. Its value depends on the type of mother wavelet and in the present case it is about three. Thus, the resolution scale r and the frequency of a wavelet are related through the central frequency according to the formula: $f = F_c/r$. It can be noted that in the Fourier decomposition the projection onto trigonometric functions

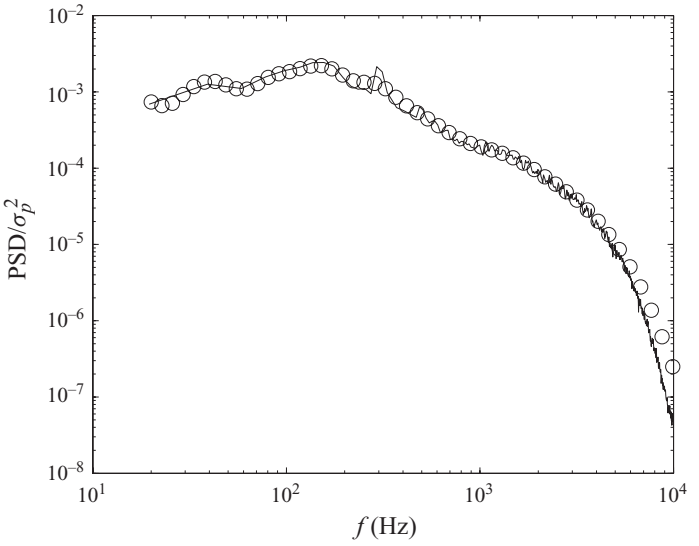

FIGURE 1. Power spectrum obtained from the wavelet transform performed using a Battle–Lemarie kernel (○○○), compared with a standard Fourier spectrum (———). The signal considered is taken from a pressure probe in the tip region and in the reference configuration described in § 3. The spectra are normalized with respect to the signal's standard deviation (σ_p).

spreads the physical information over a theoretically infinite time domain. Localized events are therefore ill-represented by the Fourier domain especially when the Fourier transform is assessed numerically, while they are correctly retrieved by the wavelet transform through the representation of the signal over a two-dimensional map in the time-resolution scale domain.

Formally, the wavelet transform of a signal $p(t)$ at the resolution time scale r is a complex-valued function given by the following expression:

$$w(r,t) = C_\Psi^{-1/2} \int_{-\infty}^{+\infty} \Psi^* \left(\frac{t-\tau}{r} \right) p(\tau)\, \mathrm{d}\tau, \tag{2.1}$$

where $C_\Psi^{-1/2}$ denotes a coefficient which accounts for the mean value of $\Psi(t)$, and the integral represents a convolution between $p(t)$ and the dilated and translated complex conjugate counterpart of $\Psi(t)$.

The event tracking method used therein is based on the computation of the so-called local intermittency measure (LIM; Farge 1992) defined as

$$\mathrm{LIM}(r,t) = \frac{w(r,t)^2}{\langle w(r,t)^2 \rangle_t}, \tag{2.2}$$

where the symbol $\langle \cdot \rangle_t$ denotes a time average. This function enhances non-uniform distributions of energy in time, since the quantity $w(r,t)^2$ can be interpreted as the energy contained in the signal at the scale r and the instant t. The standard Fourier energy spectrum can be recovered by simple time integration of $w(r,t)^2$ and related to the power spectrum. An example of the wavelet reconstructed Fourier spectrum plotted against the standard power spectrum is shown in figure 1. Similar results can be obtained by using different wavelet kernels (Farge 1992), demonstrating that the choice of the wavelet type does not influence the results.

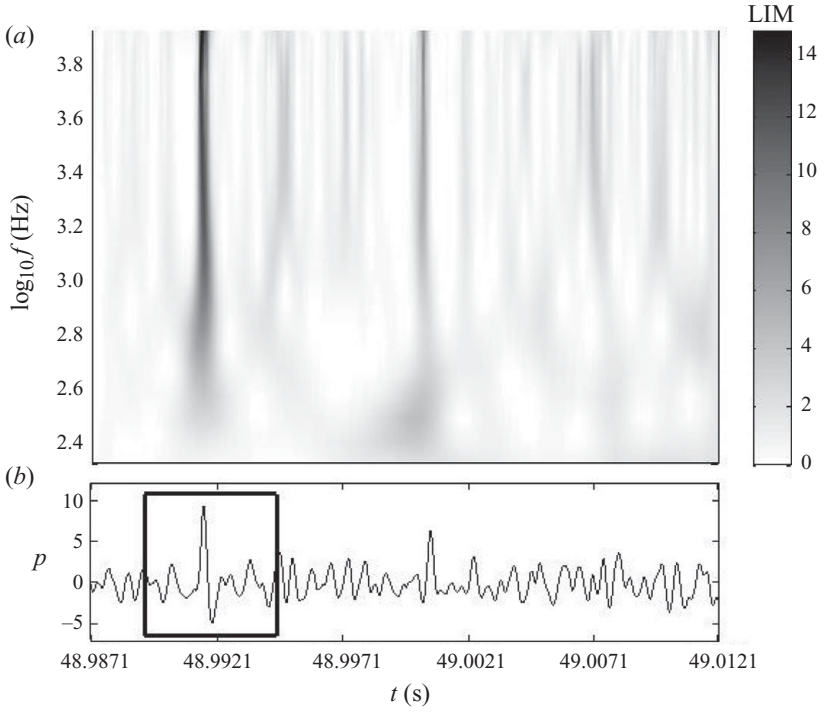

FIGURE 2. Example of selection procedure: (*a*) the large value of LIM indicates that an event occurs at the probe location in $t_0 \sim 48.992$ s. Once the event is detected the portion of pressure signal (*b*) centred on t_0 is extracted to perform the conditional average. The signal considered is taken from a pressure probe in the tip region and in the reference configuration described in § 3.

As originally introduced by Camussi & Guj (1997), the LIM amplitude at a selected scale r can be thresholded in order to collect a set of events and to determine how their appearance is distributed in time. For a given scale $r = r^*$, LIM as a function of time can be analysed and a proper trigger threshold level T can be fixed. When, for $t = t_0$, $LIM > T$, it may be assumed that a particular type of pressure event has been detected at the time instant $t = t_0$ at the scale $r = r^*$. By varying the trigger amplitude, one can select events of different levels of energy, whereas for $r < r^*$ one can observe fluctuations corresponding to smaller resolutions (or larger frequencies). In view of the LIM definition, the events extracted from the thresholding procedure will be denoted as high pressure/energy events. It has been checked that, except for the far-field PIV conditioning, by varying the wavelet resolution scale r^* at which the LIM events are selected, no significant variations of the averaged structures occur. The only effect is a variation of the signal-to-noise ratio correlated to the lack of statistical convergence when the events are selected at large scales (corresponding to a low resolution of the adopted wavelet). The weak influence of the scale where the threshold is applied is due to the fact that the wavelet transform of time localized events entails a large number of scales (see e.g. Kevlahan & Vassilicos 1994). This can be clearly seen in figure 2, where an example of LIM computed from a wall pressure signal is presented. A small resolution scale is usually selected for the LIM thresholding (see also Camussi & Guj 1997). With respect to large scales, this choice ensures a better time resolution during the event detection as well as a greater number of detected events and thus a better statistical convergence.

Concerning the choice of the threshold level, two conditions have to be satisfied: the threshold must be high enough to detect only the most energetic events, but not too high, so that enough events are detected and the statistical convergence is reached. It has been checked that, according to previous works (since Camussi & Guj 1997), the threshold can be chosen in a broad range of values without changing significantly the result. In the present approach, the level has been set to be of the order of 10. Further comments on this aspect are given in § 4.

2.1. *The auto-conditioning procedure*

Once the pressure events have been selected and well localized in the time domain, a conditional average of the original pressure signal can be performed. The time signature of the pressure events can be recovered by ensemble-averaging the pressure signals centred at the instants $\{t_0\}$ when LIM overcomes the trigger threshold. If t_0 is an instant when an energy burst is detected for a certain trigger level T, we can define $p^{(T)}(t, t_0)$ as the portion of the original pressure signal centred in t_0 and extending over a time interval of proper width. In figure 2, an example of a real pressure signal and the corresponding LIM is reported to clarify the procedure. The ensemble average is then taken over all t_0 when the pressure/energy is above the trigger level, and may be written (in the continuous form) as

$$\langle p \rangle (t - t_0) = \langle p^{(T)}(t, t_0) \,|\, \{t_0\} \rangle_{t_0}, \tag{2.3}$$

which indicates that the procedure leads to a statistical averaging of the signal p conditioned on the events $\{t_0\}$.

The auto-conditioning procedure is based on the selection of events from a pressure signal and the conditional average of the signal itself. The expected result is an ensemble-averaged time signature representing the most probable shape of the most energetic structures hidden in the original chaotic signal. As we shall see in the following, the shape of the averaged signature varies depending on the position along the tip edge and the gap width, thus leading to interesting physical outcomes.

2.2. *The cross-conditioning procedure*

The conditioning method explained above may be applied to two different signals acquired simultaneously.

In the present approach, the triggering signal is always given by pressure time series measured either at the aerofoil surface or in the far field. Conversely, the conditioned signals can be pressure at the wall or velocity, either time series or two-dimensional fields, the velocity data consisting of single-point velocity time series (HWA signals) or PIV snapshots. In the case of joint HWA/pressure measurements, the outcome of the cross-conditional procedure is an averaged time signature of velocity. Conversely, the PIV/pressure conditioning delivers an averaged two-dimensional spatial velocity field which can help to address more accurate topological interpretations.

Besides, an interesting point is the possibility of individuating, statistically, the position where noise has been radiated. According to Guj *et al.* (2003), it is possible to determine a time delay between the averaged time signature and a reference time corresponding to the peaks in the triggering pressure signal. Taking into account the local convection velocity and the speed of sound c_0, it is possible to determine the spatial location of the flow structures correlated with the pressure/energy events detected either at the wall or in the far field.

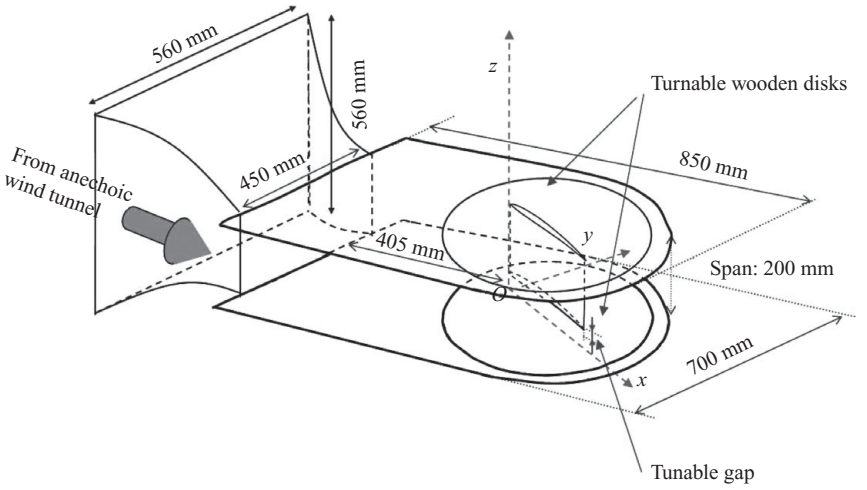

FIGURE 3. Sketch of the experimental set-up.

3. Experimental set-up

3.1. *Flow set-up*

The experiment was carried out in the anechoic room (10 m $\times$ 8 m $\times$ 8 m) of the Laboratoire de Mécanique des Fluides et d'Acoustique (LMFA), a joint CNRS–ECL–UCB Lyon I laboratory located at the Ecole Centrale de Lyon. Air was supplied by a high-speed subsonic anechoic wind tunnel with a 0.45×0.20 m^2 rectangular nozzle at Mach numbers ranging up to 0.3. The jet is flanged by two horizontal plates on the upper and lower sides of the jet and, as shown in figure 3, the aerofoil is located at $\sim$1.5 chords downstream of the jet nozzle, which has been checked to be within the potential core of the jet. The NACA 5510 aerofoil is mounted onto a turnable disk attached to the upper plate while another disk is mounted onto the lower plate. The latter either contains a square glass window for PIV and laser Doppler velocimetry (LDV) measurements, or it is equipped with microphones for wall pressure measurements in the gap region. This lower disk allows rotation of the measurement devices independently of the aerofoil. The gap h is also adjustable, spanning from 0 to 10 mm, the total height (gap + span) remaining equal to 200 mm. Since the two end plates and the aerofoil remain motionless, the gap flow is only induced by the high camber and angle of attack. This indeed results in a high load and a subsequently significant gap flow.

Different configurations are investigated even though most of the measurements presented therein will pertain to a so-called reference configuration. The various parameters characterizing this reference configuration are summarized in table 1. In order to evaluate some interesting effects, results are presented at different inflow velocities and gaps.

The coordinate system also illustrated in figure 3 is bound to the aerofoil, and is particularly useful to locate the wall pressure probes. Thus, the origin O is located at the tip of the leading edge: the x axis along the aerodynamic chord points from the leading edge to the trailing edge; the z axis follows the spanwise direction from the tip to the upper plate; the y axis is normal to the chord, pointing from the pressure to the suction side.

Aerofoil		NACA 5510
Chord c	(mm)	200
Span l	(mm)	200
Distance from nozzle	(mm)	300
Gap h	(mm)	10
Angle of attack α	(deg)	15
Inflow velocity U_0	(m s^{-1})	70 ± 1
Speed of sound c_0	(m s^{-1})	345 ± 3.5
Mach number Ma		0.203 ± 0.05
Inflow turbulence level u'/U_0		0.7 %
BL 99 % thickness δ	(mm)	$\sim$18
BL displacement thickness δ^*	(mm)	$\sim$1.4
Ambient pressure	(kPa)	98.7 ± 0.8
Ambient temperature	(K)	296 ± 6
Reynolds number Re_c		9.5×10^5

TABLE 1. Parameters of the reference configuration and main symbols.

3.2. *Measurements*

The measurements performed include a PIV, HWA and LDV characterization of the mean and fluctuating flow. The steady and unsteady pressure is also measured in the mid-span plane, in the tip region as well as in the far field. The large data set also includes a variety of joint velocity/pressure measurements. The acquired signals are analysed with standard tools of statistical analysis in order to accomplish an overall characterization of the flow behaviour. In the reference configuration ($U_0 = 70$ m s^{-1}, $h = 10$ mm, 15° angle of attack), the incoming boundary-layer thickness is $\delta = 18$ mm whereas the displacement thickness is about $\delta^* = 1.4$ mm. As shown by Grilliat *et al.* (2007), the clearance flow reaches a maximum cross-chord velocity near mid-chord where it leaves the gap at the suction side edge as a cross-flow jet that is deviated by the surrounding flow and eventually rolls up into a large tip vortex. The interaction between this vortex and the outer unperturbed flow or the aerofoil wall gives rise to two highly turbulent regions that develop downstream of the mid-chord. The flow qualification has been conducted through extensive anemometric and static pressure measurements. Figure 4 shows an example of the pressure coefficient distribution measured along the aerofoil. It must be pointed out that numerical investigations have been also conducted to validate the set-up. Specifically, numerical results have shown that the measured pressure coefficient distribution (obtained for a 15° angle of attack) can be approximated in an infinite parallel flow with a 7°–7.5° angle of attack as a result of the jet deviation. Thus, an effect of the jet width is documented but, as specified above, the aerofoil was checked to be located within the potential core of the jet flow and no interactions with the jet shear layers were present. A detailed description of the flow conditions and the adopted instrumentation is also given in Grilliat *et al.* (2007).

In this paper, these experimental data are analysed with the wavelet approach described in the previous section. For the purpose of the present work, the data sets analysed are limited to the wall pressure fluctuations, to the simultaneous HWA/pressure and to the simultaneous PIV/pressure signals. In the last two cases, pressure is measured both at the wall and in the far field.

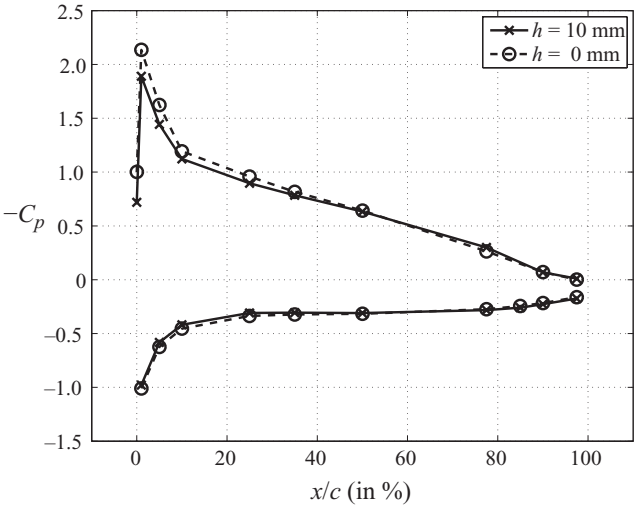

FIGURE 4. Example of pressure coefficient distribution along the pressure and suction sides of the aerofoil for the self-noise and the maximum gap configuration.

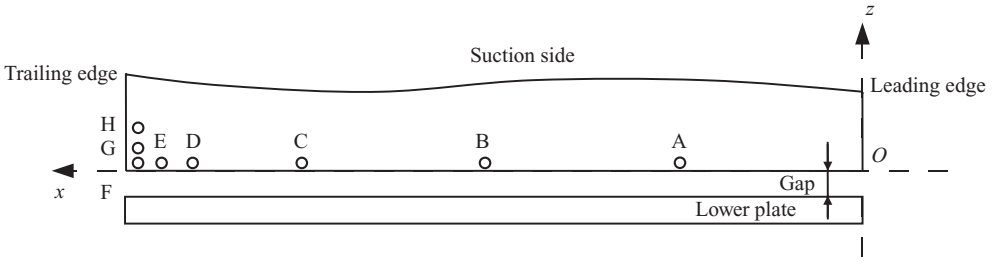

FIGURE 5. Wall pressure probe locations. The probes are located 1.5 mm above the suction side edge. Probes A, B, C, D, E and F correspond to chordwise positions $x/c = 25\,\%$, $50\,\%$, $77.5\,\%$, $90\,\%$, $95.5\,\%$ and $97.5\,\%$, respectively. Probes G and H are located at the same chordwise position as F but respectively 2 and 5 mm above into the spanwise direction.

3.2.1. *Joint HWA/pressure measurements*

Steady and fluctuating wall pressure is measured in several points of the aerofoil's surface and the lower plate. Most of the pressure probes, referred to in the present analysis as A–F, are placed on the aerofoil mainly above the aerofoil suction side tip edge ($z = 1$ mm), as detailed in figure 5. Two additional probes, I and J, are placed in the gap on the aerofoil tip in the gap region as illustrated in figure 7. They are located on the camber line at $x/c = 2.5\,\%$ and $x/c = 77.5\,\%$. Moreover, two 1/2 in. Bruel–Kjaer type 4191 far-field microphones are placed at each side of the aerofoil in the mid-span–span plane at a distance $r \sim 1.0$ m from the aerofoil centre ($c/2$, 0, 0), the observation angle with respect to the aerofoil chord being $\pm 90°$. Far-field conditions are reached typically above 350 Hz.

A specific technique is used to measure the pressure fluctuations on the surface of this relatively small aerofoil with microphones. Little pinholes ($\varnothing = 0.5$ mm) are manufactured at the measurement locations and connected to thin capillary tubes into which the microphones are flush-mounted at a remote position outside the

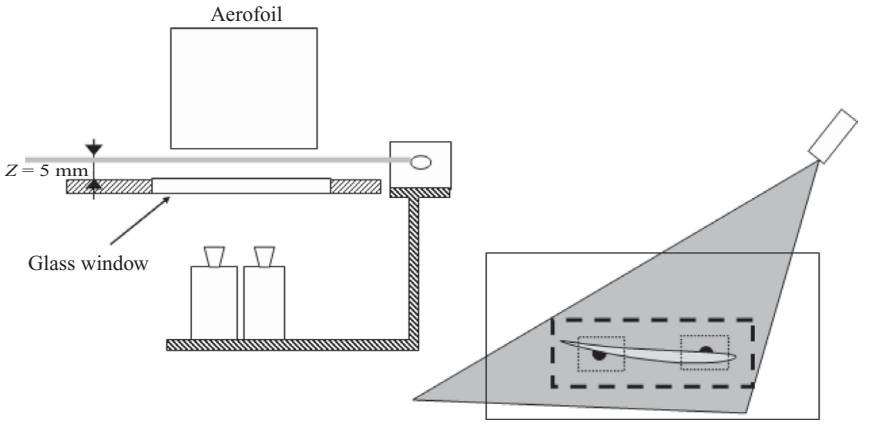

FIGURE 6. Sketch of the PIV experimental set-up.

aerofoil, where the rigid tubes open into 3 m long flexible tubes which act as anechoic terminations of the probes. The frequency response limit of the wall pressure probes was found to be about 8 kHz, and more details on this device and the calibration procedure can be found in Roger & Perennes (1998) and Arguillat (2006). The pressure fluctuations are measured with Bruel–Kjaer ICP type 4935 microphones that are pre-amplified by a PXI system for data acquisition. Data analysis is carried out with Matlab software.

The fluctuating velocity is obtained from a single hot-wire 55P11 Dantec anemometer probe mounted onto a traversing system. Systematic testing both with and without the probe is carried out to reject wall pressure data that are spoiled by the probe flow perturbations. The probe is mounted in the gap region, closely downstream of the lower end of the trailing edge ($x/c = 1.015,\ y/c = 0.01,\ z/c = 0.04$). All signals are acquired simultaneously and sampled at 64 kHz by the PXI system.

The wall pressure signals are acquired simultaneously with the hot-wire signal using the PXI acquisition system and synchronizing the acquisitions through an external trigger.

The pressure events are determined by the wavelet technique described in the previous section using orthogonal discrete Battle–Lemarie wavelets (see Camussi & Guj 1997). By appropriately windowing the pressure time series (Meneveau 1991), the wavelet expansion is performed over segments of 4096 samples. In view of the dyadic arrangement of the wavelet coefficients, the segment length corresponds to a range of 12 degrees of resolution (scales).

3.2.2. *PIV/pressure measurements*

The PIV set-up consists of a LaVision system which is associated with two CCD cameras (35 mm focal length lenses) and controlled by LaVision's software DaVis. A double laser sheet is generated in a plane parallel to the lower plate (that is, at fixed z position) via two coupled laser YAG cavities. The two cavities emit successive light pulses which are directed onto a same plane measurement region. A sketch of the laser sheet is shown in figure 6. The two cameras are placed beneath the lower plate which is equipped with a glass window. The cameras are located next to each other in order to provide pictures from the whole aerofoil with a good resolution.

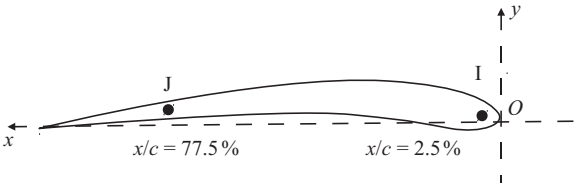

FIGURE 7. Side view of the tip edge of the aerofoil: position of the two pressure taps in the joint PIV/pressure measurements.

As sketched in figure 6, the laser and the cameras are fitted on a common support that can be moved up and down: thus, measurements at any spanwise position (z coordinate) can be performed without tuning the laser/camera system. For the PIV/pressure simultaneous measurements discussed in the present work, the gap is 10 mm and the measurement plane was in the mid-gap plane (5 mm away from the tip edge of the aerofoil), the laser source being placed on the pressure side.

In this configuration, the measurement window is a 250×105 mm^2 rectangle rotated by 6.2° with respect to the (O, x) direction around the z axis about the aerofoil centre $(c/2, 0, 0)$. Each camera has a 1280×1024 pixel resolution, and the velocity fields are computed using a 32×32 pixels interrogation window that corresponds to a 1.5×1.6 mm^2 area in the image with 50 % overlap. Since the flow is highly three-dimensional in the gap region, the delay between two images was kept very short (between 5 and 15 μs) to keep track of as many particles as possible. The seeding particles are obtained from vaporized paraffin oil that is injected upstream of the wind-tunnel fan.

The acoustic signal is obtained from the suction side 1/2 in. microphone described in § 3.2.1, which is now moved 1.5 m away from the aerofoil centre in the cross-chord direction (y). Far-field conditions are now reached above 250 Hz. The wall pressure signals are measured in the gap with probes I and J (see § 3.2.1 and figure 5).

The measurements are divided into 10 acquisition series. During each acquisition, 60 PIV snapshots are taken at a frequency of 1 Hz (which means 60 s per acquisition), while the pressure signals are sampled at 20 kHz. This yields a total of 600 PIV snapshots and 10 pressure time series.

In order to improve the accuracy in the present case where only few data are available, the pressure signals are processed by using a continuous complex wavelet expansion, to achieve a more accurate time–frequency resolution. Once the pressure events are extracted, the conditional analysis is carried out by averaging the PIV snapshots corresponding to the selected time slots of the pressure/energy events, according to the procedure described in the previous section.

4. Results

The results presented hereafter are organized according to the nature of the signal chosen as a trigger in the conditioning procedure. In the first part of the paragraph, the trigger is given by wall pressure signals. In the second part, acoustic effects are analysed since the events used as a trigger are determined from the far-field pressure fluctuations. For the sake of clarity, a summary of the analysed flow conditions, including a description of the signal types, is given in table 2.

Test case	Configuration	Conditioning	Trigger signal	Conditioned signal
1	$h = 0$–10 mm, $U_0 = 70$ m s^{-1}	Auto	Wall pressure along the tip edge	Wall pressure along the tip edge
2	$h = 10$ mm, $U_0 = 20$–90 m s^{-1}	Auto	Wall pressure along the tip edge	Wall pressure along the tip edge
3	$h = 10$ mm, $U_0 = 70$ m s^{-1}	Cross	Wall pressure at $x/c = 0.775$ on the tip edge ($z/c \simeq 0$)	Wall pressure along the tip edge
4	$h = 10$ mm, $U_0 = 20$–90 m s^{-1}	Cross	Wall pressure at $x/c = 0.775$ on the tip edge ($z/c \simeq 0$)	Wall pressure along the tip edge
5	$h = 0$–10 m, $U_0 = 70$ m s^{-1}	Cross	Wall pressure along the tip edge	Velocity time series just over the TE at the tip ($x/c = 0.975$, $y/c = 0.009$, $z/c = 0.025$)
6	$h = 10$ mm, $U_0 = 70$ m s^{-1}	Cross	Wall pressure at $x/c = 0.775$ at the tip facing	PIV velocity fields in the mid-gap plane
7	$h = 10$ mm, $U_0 = 70$ m s^{-1}	Cross	Far-field pressure	Wall pressure along the tip edge
8	$h = 10$ mm, $U_0 = 70$ m s^{-1}	Cross	Far-field pressure	PIV velocity fields in the mid-gap plane

TABLE 2. Summary of the test cases analysed in the present work.

4.1. *Wall pressure conditional statistics*

4.1.1. *Wall pressure auto-processing*

The ensemble-averaging procedure defined as auto-conditioning procedure in § 2 is applied to the whole set of measured wall pressure signals providing the wall pressure-averaged signatures in several positions over the aerofoil surface. As shown in figures 8–10, the conditioning procedure applied to signals recorded in the vicinity of the tip (test case 1 of table 2) clearly reveals an averaged time signature whose shape varies as an effect of the position and the gap width. An overall view of the shape variation as an effect of the position along the tip is given in figure 8 while figure 9 depicts shape details of the averaged structures. It is possible to note that the averaged time signatures exhibit strong oscillations as an effect of the leakage flow, in the vicinity of the gap the oscillations being more pronounced close to the trailing edge and at the aerofoil tip. Figure 10 shows that the amplitude of the oscillating averaged pressure signature becomes larger as the gap increases, while the angle of attack and the inflow velocity are kept constant. The observed oscillations are not due to periodic phenomena but due to intermittent packets which are masked by background random fluctuations. A physical interpretation of this phenomenon can be found in the roll-up mechanism of the vortical structures shed intermittently from the suction side tip edge of the aerofoil. It has been checked on other results not reported here for the sake of brevity, that the events revealed by figure 10 are indeed related to the gap. It has also been checked that the observed results were not related to the choice of the parameters adopted into the wavelet-based conditioning

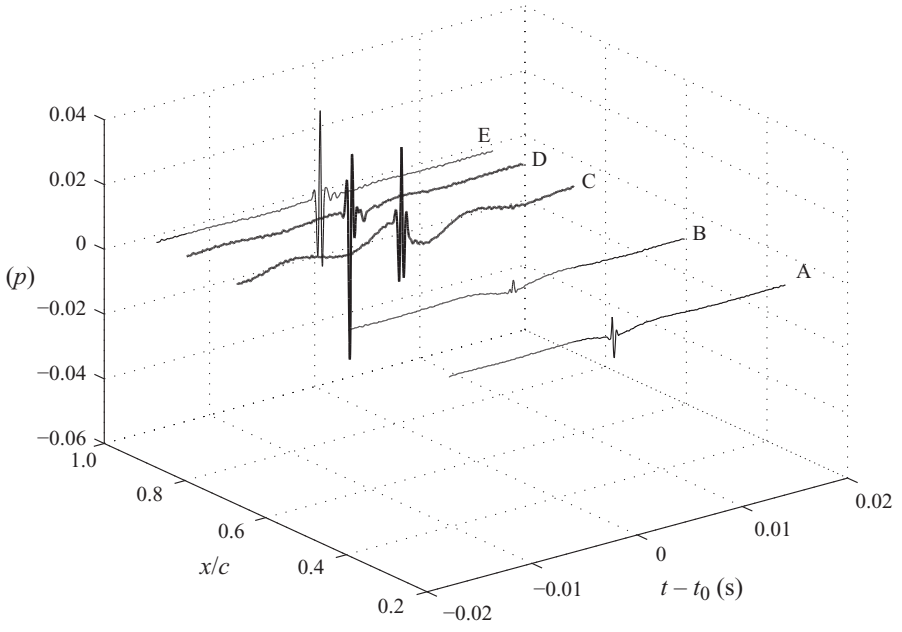

FIGURE 8. Averaged pressure time signatures obtained for several chordwise positions in the tip region ($z/c = 0.005$) for the reference gap configuration. From right to left: probe A ($x/c = 0.25$), probe B ($x/c = 0.50$), probe C ($x/c = 0.775$), probe D ($x/c = 0.90$) and probe E ($x/c = 0.955$).

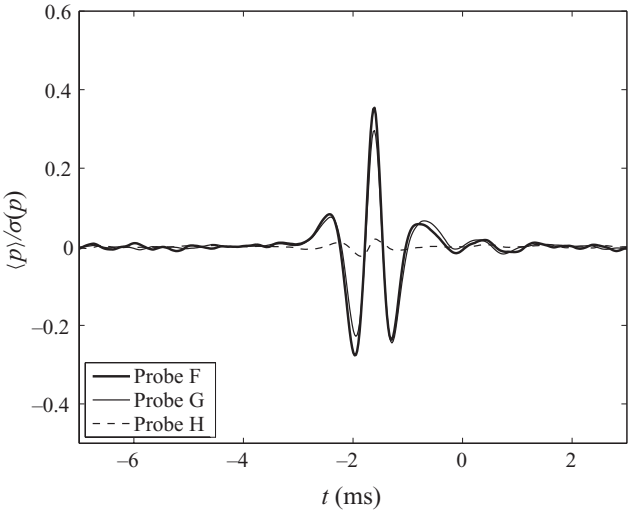

FIGURE 9. Averaged pressure time signatures obtained in the trailing-edge region ($x/c = 0.975$) for the reference gap configuration: effect of the distance from the gap (z): probe F ($z/c = 0.005$), probe G ($z/c = 0.015$) and probe H ($z/c = 0.03$). The amplitudes are normalized with respect to the standard deviation of the original signals (σ_p).

procedure. For instance, it has been checked that the choice of the threshold level adopted into the events selection procedure was not influencing the shape of the averaged structures, and an explanatory example in this sense is given in figure 11.

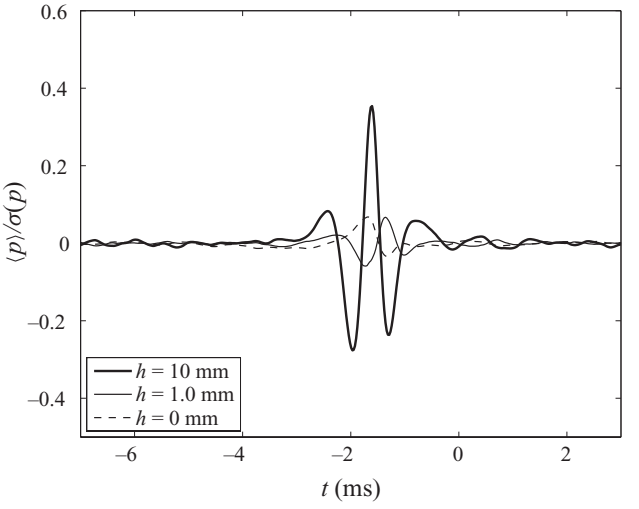

FIGURE 10. Averaged pressure time signatures obtained in the trailing-edge region at the tip edge (probe F: $x/c = 0.975$, $z/c = 0.005$): effect of the gap width, with U_0 and α kept at their reference values. The amplitudes are normalized with respect to the standard deviation of the original signals (σ_p).

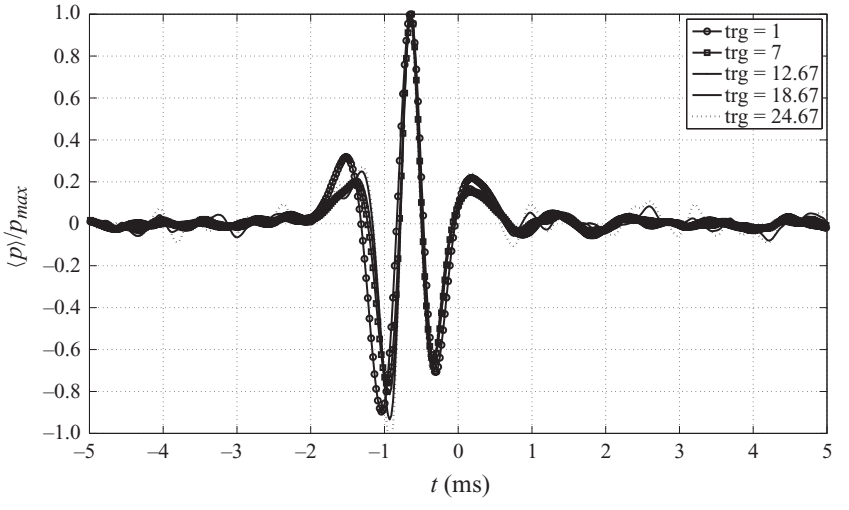

FIGURE 11. Averaged pressure time signatures obtained from probe F for different threshold levels adopted in the conditioning procedure (see § 2). The results are normalized in order to evidence any difference in the shape of the averaged structures. Trg, trigger.

As a further check, a statistical analysis of the waiting time between consecutive wall pressure events has also been performed by computing the probability distribution function (p.d.f.) of the time delay $\Delta t^i = t_0^i - t_0^{i-1}$, $\{t_0\}$ being the set of time instants corresponding to the peaks in the wall pressure LIM. The p.d.f. of the waiting times measured in the tip region is reported in figure 12. The p.d.f.s exhibit exponential tails that appear linear on the semilog plot and are quite similar to those reported for swirling flows in the literature (see e.g. Abry *et al.* 1994). The exponential distribution of the waiting time is typical of Poisson statistics of uncorrelated events. From a

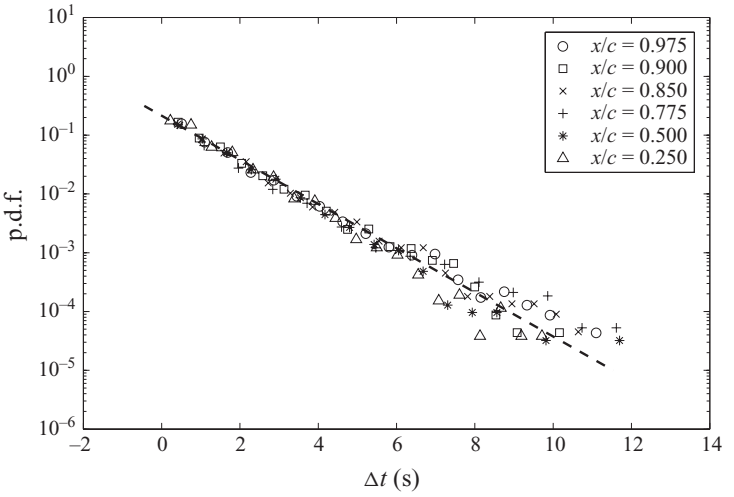

FIGURE 12. P.d.f. of the time delay Δt between consecutive pressure events. The dashed line represents a pure exponential decay of the form $y = \exp(-0.98x)$.

physical viewpoint, the exponential decay indicates that the selected pressure events can be considered statistically independent from each other. A satisfactory collapse of the p.d.f.s can be appreciated, suggesting that such a behaviour is an intrinsic property of the analysed random variables. The results in figure 12 further confirm the reliability of the adopted identification method, which allows for separation of coherent intermittent fluctuations from the background. They also confirm that the oscillatory behaviour observed in the averaged time signatures above presented is due to physical events characterized by an intermittent statistics. Background Gaussian fluctuations or periodic spurious oscillations, if present, should in fact modify the nature of the selected events and alter significantly the shape of the waiting time p.d.f. from the observed pure exponential decay.

The upstream velocity has been varied from 20 to 90 m s^{-1} in order to unveil the dependence of the time signature with respect to the flow conditions. The corresponding results of the wall pressure auto-conditioning retrieved from probe F, which is located on the suction side tip trailing-edge corner, are presented in figure 13 (test case 2 of table 2).

Each averaged signal is centred with respect to its convection time and plotted with respect to $t \times U_0^{0.5}$. The choice of this time scaling is clear from the resulting curves: it appears that the conditioned signals for a given probe have a constant width regardless of the velocity. This means that the typical time duration of the events scales with $1/U_0^{0.5}$. A physical interpretation is proposed using a potential vortex model. Let us consider a potential vortex convected along a rigid plane ($y = 0$) in a two-dimensional steady flow at a uniform velocity U_0 in the x direction. If z denotes the complex number $x + \mathrm{i}y$, the complex potential of the resulting flow is given by

$$\phi(\zeta) = U_0 z + \Gamma_0 \ln(\zeta - \zeta_0) - \Gamma_0 \ln(\zeta - \zeta_0^*), \tag{4.1}$$

where Γ_0 and ζ_0 are the circulation and the position of the vortex, respectively, and the asterisk ($*$) denotes the complex conjugate. The third term is the image of the vortex due to the presence of the plane. As a result, the potential vortex convects

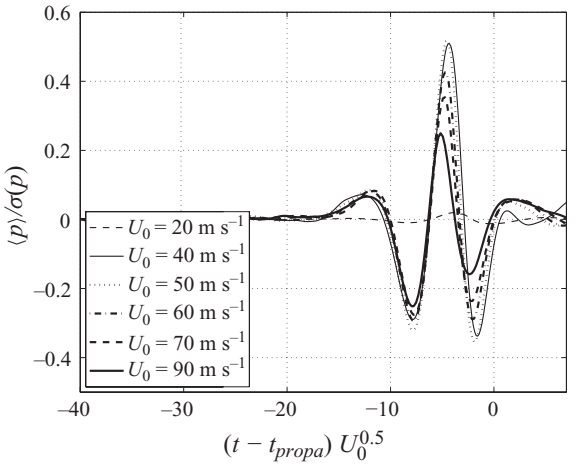

FIGURE 13. Auto-conditioned signals at probe F ($x/c = 0.975$, $z/c = 0.005$). The averaged signals are plotted with respect to $t \times U_0^{0.5}$ and the amplitudes are normalized with respect to the standard deviation of the original signals (σ_p).

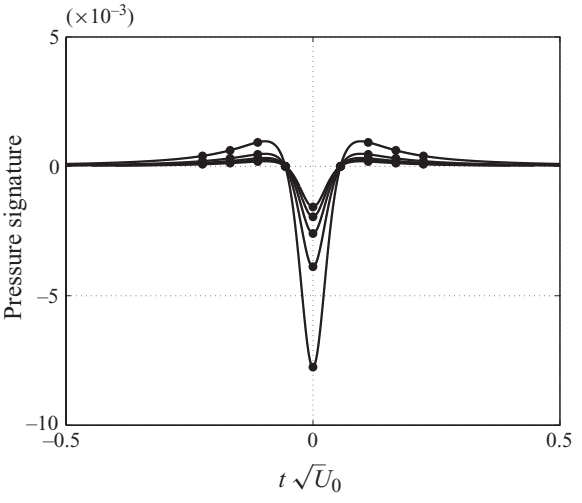

FIGURE 14. Pressure signature on a virtual probe located at $\zeta_1 = 0$ (the symbols on the lines correspond to non-dimensional time steps $t \times U_0/b$. These signatures are plotted with respect to $t \times U_0^{0.5}$.

along the wall at a constant distance $b = \mathrm{Im}(\zeta_0)$ and a constant velocity U_c. In the adopted model the convection velocity is given by the following expression:

$$U_c = U_0 + \frac{\Gamma_0}{4\pi b}. \tag{4.2}$$

The pressure generated at the wall is computed via Bernoulli's theorem during the vortex passage. A simulation for four different values of U_0 is given in figure 14. Several computations are carried out, whereby the velocity U_0 and b are increased by factors a and $\sqrt{a}$, respectively, with a varying from 1 to 5. The pressure signatures

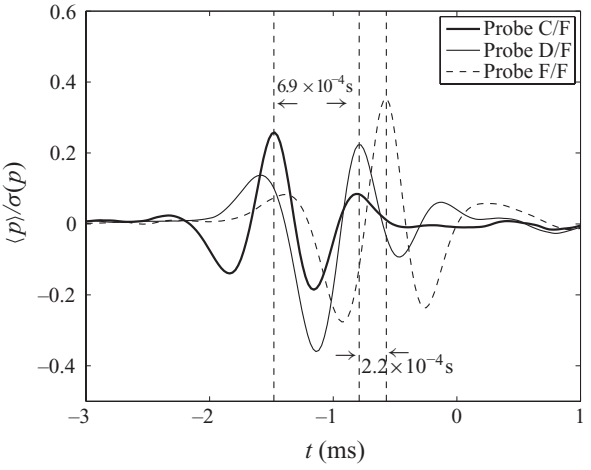

FIGURE 15. Pressure cross-conditional correlation in the tip region for the reference gap configuration. The amplitudes are normalized with respect to the standard deviation of the original signals (σ_p).

are plotted in figure 14 with the scaled time $t \times U_0^{0.5}$. Two conclusions can be drawn from this little exercise.

(i) The time scaling is appropriate for this elementary vortex. This scaling is a side effect of the competition between potential and convective effects of the vortex, as it involves the velocity U_0 and the vortex-to-wall distance.

(ii) As a result, the events tracked by the wavelet-based auto-conditioning method may be driven by similar physics as near-wall vortices since the scaling is the same in both cases. However, the shape of the wavelet-filtered pressure signature is not similar to that of the convected vortex. Computations of more complex vortex systems (a co-rotating vortex pair) seem to show a better agreement as far as the shape is concerned (see Grilliat *et al.* 2008). In the tip flow, there are typically two co-rotating vortices shed each by one edge of the tip. Since the vortex motion is three-dimensional in the real tip flow, these potential models may just be regarded as indicators of the physics that may lie behind the conditional wavelet results.

4.1.2. *Wall pressure cross-conditional statistics*

As mentioned in § 2, the wall pressure cross-conditional analysis also allows us to track the most energetic events across the tip flow region. In fact, coherent pressure fluctuations detected in different locations on the wall might either be generated by independent fluid dynamic/acoustic perturbations or originate from the same perturbation which convects or radiates to the position where they are detected. The cross-conditioning is carried out in the aerofoil tip region (test case 3 of table 2) and with the probes shown in figure 5.

Figure 15 shows the results of the cross-analysis conducted on the pressure signals in the tip region. The pressure signal recorded at probe F is used to trigger the time series provided by the pressure probes in C and D. It may be seen that the averaged pressure signatures preserve the same shape, but a time shift is revealed moving downstream. Due to the three-dimensional nature of the flow in the gap region, a convection velocity cannot be determined accurately and a direct relationship with the free-stream velocity cannot be delivered. Further discussions on this aspect are given below.

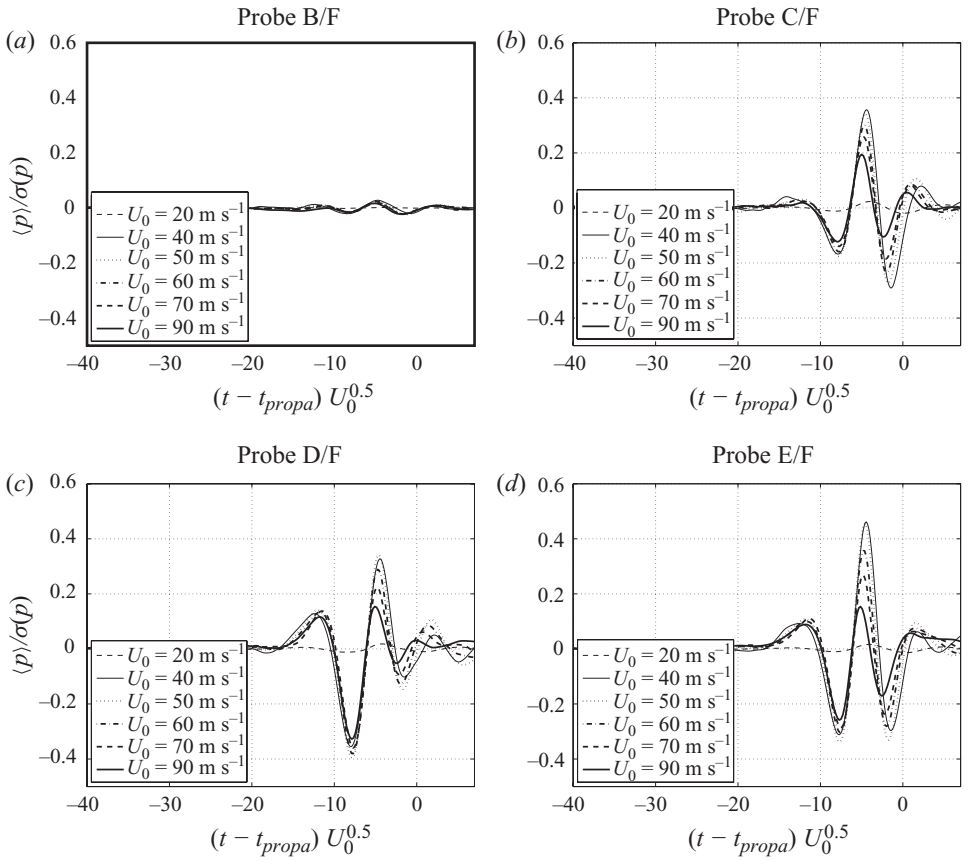

FIGURE 16. Pressure cross-conditional correlation in the tip region. Results for probes B–E. The averaged signals are centred on the convection time and multiplied by $U_0^{0.5}$. The amplitudes are normalized with respect to the standard deviation of the original signals (σ_p).

As for the auto-conditioning study, further cross-conditioning analyses are carried out to determine the effect of the free-stream velocity magnitude which is varied from 20 to 90 m s^{-1} (test case 4 of table 2). A summary of the results obtained is given in figure 16. As for the case of figure 13, the time scaling is $t \times U_0^{0.5}$. A satisfactory collapse of the signatures' time scale is observed, confirming the findings reported in figure 13. It can be observed that results for probes C, D and E have much larger amplitudes than the other (probe B). This is related to the tip leakage detachment position, that is, the position where the tip leakage flow is strongest. According to the results shown above, such a position is found to be located downstream of probe B.

4.1.3. *Single-point velocity/wall pressure conditional statistics*

Simultaneous velocity/pressure measurements have been performed in test case 5 (see table 2) by placing a single hot-wire probe close to the aerofoil trailing-edge corner.

The conditional statistics between the velocity signals and the pressure peaks detected for different pressure probe positions along the tip are explored in the maximum gap configuration (figure 17). Fluctuations are observed on the averaged velocity signals. These fluctuations are in phase opposition with respect to the fluctuations observed on the averaged pressure signals (figure 13). The phase

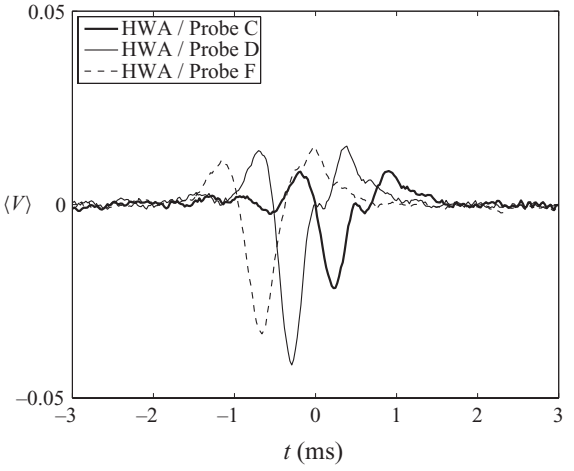

FIGURE 17. Pointwise pressure/velocity correlation in the tip edge region ($z/c = 0.005$) for the reference gap configuration using the pressure signal at probes C, D and F (located at $x/c = 0.775,\ 0.900,\ 0.975$, respectively) used as a trigger. The hot wire is set at $x/c = 1.02$, $y/c = 0.04$, $z/c = 0.04$.

opposition is very difficult to interpret as the anemometer uses a single hot wire, but it shows the existence of a causal link between the velocity perturbations and the wall pressure fluctuations in the gap suction side region, which proves that these perturbation are due to the same flow structures. Since the sign of the velocity fluctuations measured by the hot wire is the sign of the fluctuation component that is parallel to the local mean flow direction, one could argue that the phase opposition might be due to a local reverse motion as a confirmation of the strongly three-dimensional nature of the flow in this region.

4.1.4. *PIV/wall pressure conditional statistics*

The joint analysis of PIV measurements (discussed in § 3) and of single-point pressure measurements is performed only for the reference gap configuration and is included as test case 6 in table 2. On the basis of the HWA/wall pressure analysis presented in § 4.1.3, we may expect the pressure signals recorded by probe J placed at $x/c = 0.775$ (see figure 7) to provide the most useful data for the conditional PIV/wall pressure analysis. The present investigation focuses primarily on this pressure signal that, once treated with the wavelet method, provides the set of instants from which the corresponding PIV velocity fields are selected.

As stated in § 3, 60 PIV snapshots are available from each 60 s acquisition series. This represents a basic constraint to take into account, as it is evident that only some of the instantaneous velocity fields captured by these 60 snapshots could be selected. Thus, the wavelet transform of the pressure signal is performed over segments centred onto the PIV acquisition times (see e.g. figure 18). The selection of a PIV field occurs only when the LIM peak is at the origin of the time axis.

The search for an averaged structure is accomplished by ensemble-averaging the set of selected velocity fields. The selection procedure, applied to all the 10 acquisition series, provided a total of 119 pressure events, which is a small number for statistical purposes. As already pointed out above, it must be noted that the achieved PIV-averaged result is not dependent upon the wavelet resolution scale at which the LIM events are selected.

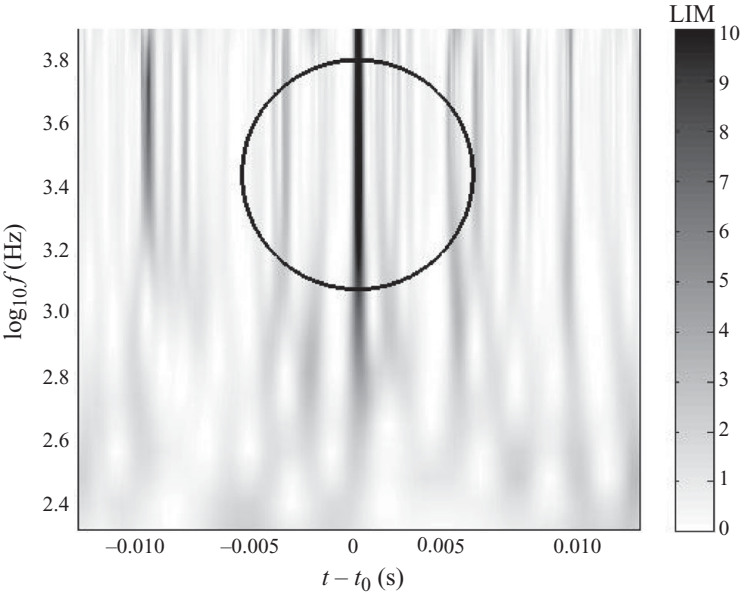

FIGURE 18. An example of a high-frequency pressure event (evidenced by the black circle) detected in the wavelet time–frequency domain from the pressure probe J ($x/c = 0.775$), in the reference configuration.

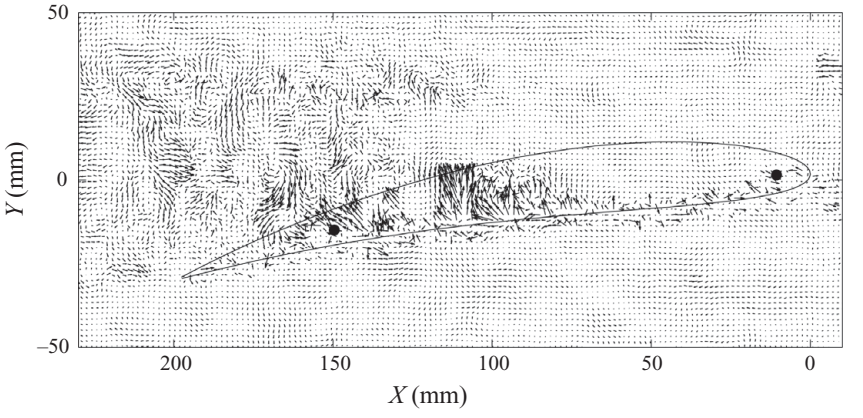

FIGURE 19. Averaged tip-flow field statistically related to the largest high-frequency pressure fluctuations on probe J. The black circles denote the pressure probes I and J ($x/c = 0.025$ and 0.775, respectively).

The achieved ensemble-averaged field is shown in figure 19. In the region upstream of the pressure probe position, very close to the location where the source is supposed to be, a fluid structure is revealed. It is located about 110 mm from the trailing edge, which corresponds to $x/c = 55$, consistent with the major outcomes presented above. From the physical viewpoint, this event seems to consist of a motion of the fluid from the pressure side of the aerofoil towards the suction side with some local swirl and reverse motion. Actually, since the PIV snapshots are taken in the mid-gap plane, the figure shows the corresponding two-dimensional cut of a three-dimensional turbulent structure. One may assume such a structure to be associated with a roll-up phenomenon occurring at the tip edge of the aerofoil, but an exact topological

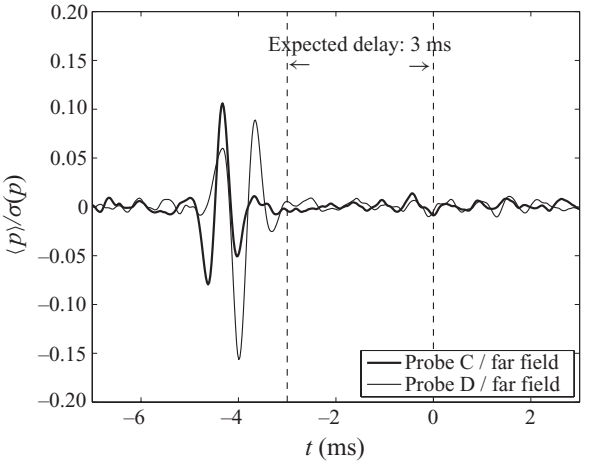

FIGURE 20. Averaged wall pressure time signature for transducers in the tip region ($z/c = 0005$) of the reference gap configuration (probe C: $x/c = 0.775$; probe D: $x/c = 0.9$) and with the far-field signal used as a trigger. The amplitudes are normalized with respect to the standard deviation of the original signals (σ_p).

interpretation cannot be proposed unless a cross-sectional analysis of the flow is performed.

4.2. *Far-field pressure conditional statistics*

4.2.1. *Far-field/wall pressure conditional statistics*

A first attempt to localize the position at which sound is generated consists of triggering the wall pressure signals with the LIM peaks detected in the far field. As explained in § 2, such a cross-analysis provides a statistical view of the time delay between the coherent wall pressure fluctuations and the largest acoustic perturbations in the far field. A wall pressure signal recorded in the region where noise is generated should provide, once conditioned by the far-field trigger, an averaged time signature whose time delay approximates the time needed for the pressure perturbation to cover the distance from the wall to the far-field microphone position.

In the present analysis, the far-field microphone is placed about 1 m away in the y direction facing the suction side at mid-chord. The conditional wavelet analysis is applied to the reference configuration with data collected from test case 7 of table 2. Assuming the speed of sound to be 340 m s^{-1}, the propagation of sound from any point of the aerofoil tip suction side to the far-field microphone is expected to last for about 3×10^{-3} s. Convection and refraction effects are negligible since the propagation from the aerofoil to the far-field microphone is almost normal to the flow for all positions along the aerofoil. As a consequence, propagation delays differing significantly, say, by more than 10 %, from 3×10^{-3} s, can be attributed to variations of the source positions. Thus, one might identify the most probable source location on the aerofoil suction side. This location is not expected to coincide with the location the radiating aerodynamic events originate from (i.e. on the aerofoil tip in the mid-chord region).

Results for probes C, D, E and F located at $x/c = 77.5\,\%, 90\,\%, 95.5\,\%$ and $97.5\,\%$, respectively, are shown in figures 20 and 21. Note that the (negative) time shift exhibited by the averaged pressure signal at $x/c = 0.775$ is quite different from the reference value: it is about 3.8 ms for probe C and decreases in the downstream

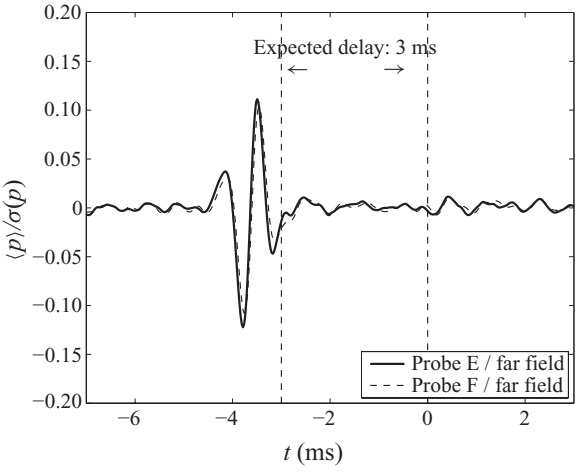

FIGURE 21. Averaged wall pressure time signature for transducers in the tip region ($z/c = 0005$) of the reference gap configuration (probe E: $x/c = 0.955$; probe F: $x/c = 0.975$) and with the far-field signal used as a trigger. The amplitudes are normalized with respect to the standard deviation of the original signals (σ_p).

position. Near the trailing edge it is very close to the reference value. This clearly shows that the selected perturbations already felt by probe C radiate sound as they reach the tip trailing-edge corner. The additional time shift observed for probe C (0.8 ms) corresponds to a mean convection velocity of about 56 m s^{-1} ($\pm$4.5 %). Note that the precision can be seen in figure 15, where the averaged signatures of 2 mm distant probes seem to overlay quite well whereas they should be delayed by 0.03 ms. This source diagnosis is not only supported by a more classical analysis discussed by Jacob *et al.* (2010) but is also consistent with classical aeroacoustic theories (e.g. Ffowcs Williams & Hall 1970; Crighton & Leppington 1971; Amiet 1976; Howe 1978) which predict a maximal radiation as turbulent structures are convected past discontinuities: an interpretation in this spirit has been proposed by Grilliat *et al.* (2008) for the tip noise source. As far as the relative amplitudes of the conditional averages are concerned, it can be concluded that despite slight differences they are quite similar. This supports the assumption that the events radiating near the trailing edge are present in the whole tip region.

4.2.2. *PIV/far-field conditional statistics*

The PIV/far-field pressure conditional analysis reported in table 2 as test case 8 is performed in order to identify the gap flow perturbations which are responsible for the sound radiation. Accounting for the time shift issue discussed in § 4.2.1, a delay between the PIV snapshot and the LIM computation of the trigger signal is fed into the conditioning procedure. In fact the optimal delay giving the strongest causal link between the PIV and the far field is determined and found to be about 4.5 ms. By extrapolating the observations from § 4.2.1, this delay should correspond to structures located at mid-chord or even upstream, given the fact that the maximal velocity reached in the gap is about 50 % above the free-stream velocity (according to Grilliat *et al.* 2007).

In contrast to the results presented in previous sections, the present conditional analysis appeared to depend moderately upon the wavelet resolution. This might be not only due to the fact that the signal-to-noise ratio of the far field is quite low but

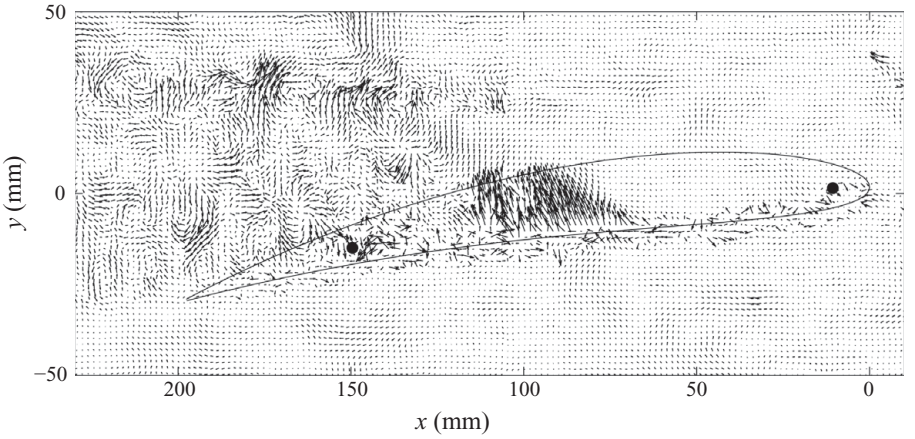

FIGURE 22. Averaged tip-flow field statistically related to the largest high-frequency pressure fluctuations in the far field.

also due to the small number of selected events available for the analysis. As discussed by Grilliat *et al.* (2007), the tip leakage noise competes with other comparable sources, such as the aerofoil trailing-edge noise and other spurious sound sources, especially at lower frequencies. Therefore, the conditional analysis illustrated in figure 20 is based on high-frequency wavelet components selected between 3 and 10 kHz.

Figure 22 shows the conditionally averaged flow field in the mid-gap plane ($z = -5$ mm), which confirms the presence of a large swirling flow region that is mainly concentrated in the gap near mid-chord, say between 40 % and 60 % chord typically. According to figure 20, the onset of these flow perturbations seems to be linked to the pressure side tip edge separation. This spatial picture is consistent with the observed time delays as well as with other observations: according to Grilliat *et al.* (2007) this part of the clearance flow also corresponds to the region where the gap cross jet reaches its maximal cross-chord velocity. It can also be seen in figure 20 that in the region facing the suction side between 50 % chord and the trailing edge, other smaller turbulent eddies are also causally linked to the far field. This illustrates the spatial coherence reached by these sound radiating structures and shows that they extend over the whole region occupied by the tip vortex. This confirms the conclusions of the conditional analysis along the suction side tip edge which showed that perturbations selected outside the gap remain coherent downstream of the mid-chord position (see figure 14), that is, downstream of the location where the tip clearance jet exits the gap.

5. Conclusions

A detailed analysis of wall pressure and velocity data measured around an aerofoil with a tip leakage flow has been presented. The analysis consists in a conditional averaging technique using a wavelet energy criterion (LIM) as a trigger on a reference signal which can be different from the averaged signal (cross-conditioning) or not (auto-conditioning). This approach allows detection of causally linked intermittent perturbations in various flow regions and assessment of their contribution to the far field. In the present study, the trigger signal is either a wall or a far-field pressure fluctuation. This approach was applied to a variety of signals retrieved from a single non-rotating aerofoil experiment carried out in anechoic conditions.

The wall pressure auto-conditioning procedure conducted in the tip region clearly reveals an averaged pressure time signature whose shape varies as an effect of the position along the tip and of the gap width.

Hence, the analysis of pressure and hot-wire signals from the suction side tip edge and its vicinity evidenced intermittent pressure or velocity perturbations along the downstream part of the aerofoil between the half chord and the trailing-edge tip. The time dependence of these perturbations was found to scale with the inverse of the square root of the velocity. By means of a simple potential model it was shown that a quite similar scaling is found for the pressure signature left by vortices sweeping along a wall. Thus, the structures found on the suction side tip edge may be associated with the vortex roll-up that starts approximately at mid-chord where the main tip leakage flow leaves the gap. The origin of these structures in the gap was determined visually by a conditional analysis of PIV measurements triggered by the tip pressure at 3/4 chord. Indeed, a causal link was found between high-energy intermittent wall pressure perturbations and intermittent turbulent structures developing in the gap between 40 % and 60 % chord typically. These swirling structures are generated by the pressure side tip edge and develop across the gap.

Finally, the intermittent flow structures evidenced by the conditional wavelet analysis were also found to contribute to the far-field radiation. By analysing the time shifts of the averaged pressure signals, it was shown that the structures generated in the gap flow actually radiate sound when they are convected past the trailing-edge tip corner. This confirms conclusions from an earlier study of the same flow where the sound power of the tip flow contribution was found to increase with the fifth power of the flow velocity which is typical for sound generation by turbulent eddies convected past an edge. The conditional PIV analysis that was conducted in the mid-gap plane and triggered by the far-field high-energy wavelet coefficients confirmed the origin of the sound radiating perturbations and their spatial extent. However, the sound radiation mechanism of the high-frequency eddies remains unclear, since the study of Grilliat *et al.* (2007) identifies a jet-like noise source.

Hence, the conditional analysis of the far-field pressure supports the idea that the phenomenon selected as the most probable responsible for the wall pressure events is also the most relevant acoustic source. The far-field wall pressure conditioning indeed suggests that the most effective acoustic source is related to the turbulent structures production area which locates approximately at the tip around $x/c \sim 0.4$–0.6. This result has been inferred from the phase-shift analysis of the wall pressure/far-field pressure cross-conditioning and has been visualized through the far-field pressure/PIV-conditioned structure.

This study has clarified some of the physical mechanisms underlying the evolution of wall pressure fluctuations and their sound generation. The mechanism identified in this academic tip clearance flow is likely to take place in more relevant configurations but might be ruled out by other perturbations such as rotating instabilities. The comprehension of those complex effects, especially for very thin gaps, remains a challenge for future studies.

This work has been funded by the European Community as part of the Sixth Framework Project PROBAND AST4-CT-2005-012222. J.G. has been partially supported by a Marie Curie Early Stage Research Training Fellowship of the European Community's Sixth Framework Programme under contract number MEST CT 2005 020301. R.C. also acknowledges partial support from Italian Ministry of Education, University and Research under a grant PRIN (2005).

REFERENCES

Abry, P., Fauve, S., Flandrin, P. & Laroche, C. 1994 Analysis of pressure fluctuations in swirling turbulent flows. *J. Phys. II* **4**, 725–733.

Amiet, R. K. 1976 Noise due to a turbulent flow past a trailing edge. *J. Sound Vib.* **47**, 387–383.

Arguillat, B. 2006 Etude expérimentale et numérique de champs de pression pariétale dans l'espace des nombres d'onde, avec application aux vitrages automobiles. PhD thesis, Ecole Centrale de Lyon, Lyon.

Bindon, J. P. 1989 The measurement and formation of tip-clearance loss. *J. Turbomach.* **111**, 257–263.

Camussi, R. & Di Felice, F. 2006 Statistical properties of large scale spanwise structures in zero pressure gradient turbulent boundary layers. *Phys. Fluids* **18**, 035108.

Camussi, R. & Guj, G. 1997 Orthonormal wavelet decomposition of turbulent flows: intermittency and coherent structures. *J. Fluid Mech.* **348**, 177–199.

Camussi, R. & Guj, G. 1999 Experimental analysis of intermittent coherent structures in the near field of a high *Re* turbulent jet flow. *Phys. Fluids* **11**, 423–431.

Casper, J. & Farassat, F. 2004 Broadband trailing edge noise predictions in the time domain. *J. Sound Vib.* **271**, 159–176.

Corsini, A., Perugini, B., Rispoli, F., Sheard A. G. & Kinghorn, I. R. 2005 Experimental and numerical investigation on passive devices for tip clearance induced noise reduction in axial flow fans. In *Seventh European Conference on Turbomachinery*, Athens, Greece.

Crighton, D. G. & Leppington, F. G. 1971 On the scattering of aerodynamic noise. *J. Fluid Mech.* **46**, 577–597.

Dunne, R. C. & Howe, M. S. 1997 Wall-bounded blade-tip vortex interaction noise. *J. Sound Vib.* **202**, 605–618.

Envia, E. 2001 Fan noise reduction: an overview. NASA TM-2001-210699.

Farge, M. 1992 Wavelet transforms and their applications to turbulence. *Annu. Rev. Fluid Mech.* **24**, 395–457.

Ffowcs Williams, J. E. & Hall, L. H. 1970 Aerodynamic sound generation by turbulent flow in the vicinity of a scattering half plane. *J. Fluid Mech.* **40**, 657–670.

Fukano, T. & Jang, C. M. 2004 Tip clearance noise of axial flow fans operating at design and off-design condition. *J. Sound Vib.* **275**, 1027–1050.

Fukano, T. & Takamatsu, Y. 1986 The effects of tip clearance on the noise of low pressure axial and mixed flow fans. *J. Sound Vib.* **105**, 291–308.

Ganz, U. W., Patten, T. J., Scharpf, D. F. & Joppa, P. D. 1998 Boeing 18-inch fan rig broadband noise test. NASA CR-1998-208704.

Goldstein, M. E. 1979 Scattering and distortion of the unsteady motion on transversely sheared mean flows. *J. Fluid Mech.* **91**, 601–632.

Grilliat, J., Jacob, M. C., Camussi, R. & Caputi-Gennaro, G. 2007 Experimental study of a tip leakage flow. Part 1. Aerodynamic and aeroacoustic measurements. In *13th AIAA/CEAS Aeroacoustic conference*, Rome, Italy. AIAA 2007-3684.

Grilliat, J., Jacob, M. C., Jondeau, E., Roger, M. & Camussi, R. 2008 Broaband noise prediction models and measurements of tip leakage flows. In *14th AIAA/CEAS Aeroacoustic conference*, Vancouver, British Columbia. AIAA 2008-2845.

Groeneweg, J. F., Sofrin, T. G., Rice, E. J. & Gliebe, P. R. 1991 Turbomachinery noise. In *Aeroacoustics of Flight Vehicles: Theory and Practice*, *Noise Sources* (ed. H. H. Hubbard), vol. 1, pp. 151–210. NASA Langley Research Center.

Guj, G. & Camussi, R. 1999 Statistical analysis of local turbulent energy fluctuations. *J. Fluid Mech.* **382**, 1–26.

Guj, G., Carley, M., Camussi, R. & Ragni, A. 2003 Acoustic identification of coherent structures in a turbulent jet. *J. Sound Vib.* **259**, 1037–1065.

Guo, Y. P. 1999 Modeling of noise reduction by flap side edge fences. In *5th AIAA/CEAS Aeroacoustic Conference*, Bellevue, WA. AIAA 99-1804.

Howe, M. S. 1978 A review of the theory of trailing edge noise. *J. Sound Vib.* **61**, 437–465.

Intaratep, N. 2006 Formation and development of the tip leakage vortex in a simulated axial compressor with unsteady inflow. PhD thesis, Faculty of the Virginia Polytechnic Institute and State University, Blacksburg, VA.

Jacob, M. C., Grilliat, J., Camussi, R. & Caputi-Gennaro, G. 2010 Aeroacoustic investigation of a single airfoil tip leakage flow. *Intl J. Aeroacoustics* **9**, 253–272.

Kameier, F. & Neise, W. 1997*a* Experimental study of tip clearance losses and noise in axial turbomachines and their reduction. *J. Turbomach.* **119**, 460–471.

Kameier, F. & Neise, W. 1997*b* Rotating blade flow instability as a source of noise in axial turbomachines. *J. Sound Vib.* **203**, 833–853.

Kevlahan, N. K. R. & Vassilicos, J. C. 1994 The space and scale dependencies of the self-similar structure of turbulence. *Proc. R. Soc. Lond.* A **447**, 238–255.

Khourrami, M. R. & Choudari, M. 2001 A novel approach for reducing rotor tip-clearance induced noise in turbofan engines. In *7th AIAA/CEAS Aeroacoustic Conference*, Maastricht, Netherlands. AIAA 2001-2148.

Ma, R. 2003 Unsteady turbulence interaction in a tip leakage flow downstream of a simulated axial compressor rotor. PhD thesis, Faculty of the Virginia Polytechnic Institute and State University, Blacksburg, VA.

Mallat, S. 1989 A theory for multiresolution signal decomposition: the wavelet representation. *Trans. IEEE*: *PAMI* **11**, 674–693.

März, J., Hah, C. & Neise, W. 2002 An experimental and numerical investigation into the mechanisms of rotating instability. *J. Turbomach.* **124**, 367–375.

Meneveau, C. 1991 Analysis of turbulence in the orthonormal wavelet representation. *J. Fluid Mech.* **232**, 469–520.

Moreau, S. & Roger, M. 2009 Back-scattering correction and further extensions of Amiet's trailing-edge noise model. Part 2. Application. *J. Sound. Vib.* **323**, 397–425.

Muthanna, C. & Devenport, W. J. 2004 Wake of a compressor cascade with tip gap. Part 1. Mean flow and turbulence structure. *AIAA J.* **42** (11), 2320–2331.

Neise, W. 1976 Noise reduction in centrifugal fans: a literature survey. *J. Sound Vib.* **45**, 375–403.

Roger, M. & Moreau, S. 2005 Back-scattering correction and further extensions of Amiet's trailing-edge noise model. Part 1. Theory. *J. Sound Vib.* **286**, 477–506.

Roger, M. & Perennes, S. 1998 Aerodynamic noise of a two-dimensional wing with high-lift devices. In *4th AIAA/CEAS Aeroacoustic Conference*, Toulouse, France. AIAA 1998-2338.

Rozenberg, Y., Roger, M., Guédel, A. & Moreau, S. 2007 Rotating blade self noise: experimental validation of analytical models. In *Proceedings of the 13th AIAA/CEAS Aeroacoustics Conference*, Rome, Italy. AIAA 2007-3709.

Storer, J. A. & Cumpsty, N. A. 1991 Tip leakage flows in axial compressors. *Trans. ASME* **113**, 252–259.

Tang, G. 2004 Measurements of the tip-gap turbulent flow structure in a low-speed compressor cascade. PhD thesis, Faculty of the Virginia Polytechnic Institute and State University, Blacksburg, VA.

Vavra, M. H. 1960 *Aero-Thermodynamics and Flow in Turbomachines*. Wiley.

Wang, Y. & Devenport, W. J. 2004 Wake of a compressor cascade with tip gap. Part 2. Effects of endwall motion. *AIAA J.* **42** (11), 2332–2340.

Wenger, C. W, Devenport, W. J., Wittmer, K. S. & Muthanna, C. 2004 Wake of a compressor cascade with tip gap. Part 3. Two-point statistics. *AIAA J.* **42** (11), 2320–2331.